Inorganic Chemistry
Article
pubs.acs.org/IC

Characterization of Phosphate and Arsenate Adsorption onto Keggin-Type Al_{30} Cations by Experimental and Theoretical Methods

Katie W. Corum, Melissa Fairley, Daniel K. Unruh, Maurice K. Payne, Tori Z. Forbes,* and Sara E. Mason*

Department of Chemistry, University of Iowa, Iowa City, Iowa 52242, United States

Supporting Information

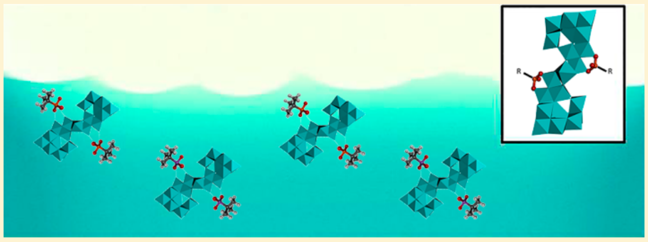

ABSTRACT: Keggin-type aluminum oxyhydroxide species such as the Al_{30} ($Al_{30}O_8(OH)_{56}(H_2O)_{26}{}^{18+}$) polycation can readily sequester inorganic and organic forms of P(V) and As(V), but there is a limited chemical understanding of the adsorption process. Herein, we present experimental and theoretical structural and chemical characterization of $[(TBP)_2Al_2(\mu_4\text{-}O_8)(Al_{28}(\mu_2\text{-}OH)_{56}(H_2O)_{22})]^{14+}$ (TBP = *t*-butylphosphonate), denoted as $(TBP)_2Al_{30}$-S. We go on to consider the structure as a model for studying the reactivity of oxyanions to aluminum hydroxide surfaces. Density functional theory (DFT) calculations comparing the experimental structure to model configurations with P(V) adsorption at varying sites support preferential binding of phosphate in the Al_{30} beltway region. Furthermore, DFT calculations of R-substituted phosphates and their arsenate analogues consistently predict the beltway region of Al_{30} to be most reactive. The experimental structure and calculations suggest a shape−reactivity relationship in Al_{30}, which counters predictions based on oxygen functional group identity.

INTRODUCTION

Aluminum is an amphoteric element that readily hydrolyzes in aqueous solution to form polynuclear species that are the building blocks of poorly crystalline and/or amorphous oxyhydroxide phases.[1−3] Initial condensation products have been identified by NMR and potentiometric measurements as soluble monomeric $(AlOH)^{2+}$, $(Al(OH)_2)^+$, $(Al(OH)_4)^-$, dimeric $(Al_2(OH)_2)^{4+}$, and trimeric $(Al_3(OH)_4)^{5+}$ complexes.[1,4−7] Larger polynuclear species can be formed upon additional titration with a hard base, forming a range of molecules that contain the Baker−Figgis−Keggin or Keggin-type structural arrangement.[3,8,9] The core feature of the Keggin-type topography is the Al_{13} tridecamer ($(Al_{13}O_4(OH)_{24}(H_2O)_{12})^{7+}$), which can be linked with additional monomers, dimers, and other oligomers to form soluble aqueous species containing 26, 30, and 32 Al^{3+} cations.[9−13] These nanoscale molecular species have been identified as the primary building unit in amorphous hydroxide solids and gels used as precursor phases in the synthesis of crystalline alumina materials and serve as a coagulant and adsorbent for contaminants in water treatment facilities.[13−20]

Phosphate and arsenate polyoxoanions are two problematic contaminants targeted during water purification processes.[21,22] Phosphorus and arsenic are both Group 15 elements that display similar chemical reactivity, but their impact on human health and the environment differ significantly. In natural systems, P(V) is an abundant and essential nutrient for humans, animals, plants, and aquatic life. Phosphorus enrichment has come under increased scrutiny due to enhanced loading in soils caused by over fertilization of agricultural lands and its role in eutrophication of freshwater systems, plant and animal deaths, and growth of toxic algae.[23] Because of its toxicity, As is considered a significant public health concern in areas worldwide, including Bangladesh, Hungary, Romania, Thailand, Mongolia, and parts of the Western United States. Human exposure occurs mostly through contaminated drinking water,[24−26] and As is classified as a known human carcinogen by the U.S. Agency for Toxic Substances and Disease Registry, as well as being on the U.S. Environmental Protection Agency (EPA) priority pollutant list.[26,27]

The exact chemical speciation of P and As is an important consideration for developing an enhanced understanding of the adsorption process and removal of these species from aqueous solutions. According to Read et al., a variety of organic and inorganic P species exist in natural water including orthophosphates, pyrophosphates, polyphosphates, and phosphonates.[28] Both P(V) and As(V) form the H_3XO_4 (X = P, As) acid in solution, deprotonating upon increasing pH to form the anionic forms. In the case of arsenic, reduction to the H_3AsO_3 and derivatization to methylarsonic acid ($CH_3AsO(OH)_2$) are quite common in natural systems.[29] According to the U.S. EPA inorganic $H_3As(III)O_4$ is more toxic than $H_3As(V)O_4$ and organic forms, but oxidation of the reduced form is the first step in removal strategies.[30] After formation of As(V), coprecipitation and adsorption reactions with aluminum and iron hydroxide phases are the primary means of removing inorganic forms from water.[31,32]

Received: May 8, 2015
Published: August 7, 2015

DOI: 10.1021/acs.inorgchem.5b01039
Inorg. Chem. 2015, 54, 8367−8374

Table 1. Selected Crystallographic Information for the $(TBP)_2Al_{30}$-S Compound

FW (g/mol)	5420.13	$F(000)$	2132
a (Å)	16.249(3)	theta range	1.36 to 26.03°
b (Å)	20.213(3)	limiting indices	$-19 < h < 19$
c (Å)	20.859(3)		$-24 < k < 24$
α (deg)	87.323(4)		$-25 < l < 25$
β (deg)	73.148(3)	ref. collected/unique	104 408/24 607
γ (deg)	73.918(3)	GOF	1.106
V (Å^3)	6295.8(16)	final R indices	$R_1 = 0.0724$
Z	1	$[I > 2\sigma(I)]$	$wR_2 = 0.2123$
ρcalc (g/cm^3)	1.120	R indices (all data)	$R_1 = 0.0886$
μ (mm^{-1})	0.324		$wR_2 = 0.2258$
crystal size (mm)	0.2 × 0.14 × 0.12	largest diff (e·A^{-3})	1.716 and −1.422

While there is widespread use of amorphous aluminum oxides as a coagulant and adsorbent, much less is known about the exact binding mechanisms of adsorbates onto the exposed surfaces. ^{31}P solid-state NMR experiments have shown that phosphate forms predominantly inner-sphere bidentate complexes on alumina, with only a few monodentate complexes observed.[33−35] Amorphous aluminum oxyhydroxide phases have been reported to have the highest adsorption rate and most rapid uptake for organic and inorganic phosphates compared to more crystalline forms.[36,37] A study by Yan et al. indicated that the identity of the adsorbed species does impact uptake and that the densities of organic phosphate on the surface of amorphous and crystalline forms of aluminum hydroxide increases with decreasing molecular weight.[15] Similar to phosphate, arsenate also forms inner-sphere bidentate and monodentate complexes on metal oxides, with bidentate complexes being predominant as shown by extended X-ray absorption fine structure (EXAFS),[38] FTIR, and XPS.[39] In terms of arsenate reactivity toward noncrystalline aluminum hydroxides, Mertens et al. investigated the removal of arsenate from contaminated water samples by Al_{13} and Al_{30} polycations and observed that 98.5−99.4% of the As(V) was removed when total aluminum concentrations were between 1 and 6 mM.[21,22,40] This study also revealed that the Al_{30} nanoclusters were the most efficient for the removal of As(V) from aqueous solutions with a nearly neutral pH, making it an excellent candidate for the purification of natural waters.

In the present study, we utilize the Al_{30} polycation ($Al_{30}O_8(OH)_{56}(H_2O)_{26}{}^{18+}$) as a model compound for phosphate and arsenate adsorption. The experimental crystal structure of $[(TBP)_2Al_2(\mu_4\text{-}O_8)(Al_{28}(\mu_2\text{-}OH)_{56}(H_2O)_{22})]^{14+}$ (where TBP = t-butylphosphonate $(CH_3)_3CPO_3$ and with the solid structure denoted as $(TBP)_2Al_{30}$-S) is reported and is used as a basis for density functional theory (DFT) calculations. Experimental data, particularly for crystallization studies, is somewhat limited to successful synthesis procedures. For example, TBP was chosen to provide steric hindrances and prevent polymerization/aggregation by the phosphate ligand so highly crystalline material could be obtained for structural characterization. Other ligands, such as methoxyphosphonate, have not successfully produced material for X-ray diffraction analysis. Similarly, arsenate and organoarsenate compounds are quite toxic and can be hazardous in material synthesis. To extend the experimental studies, DFT calculations can provide energetic and mechanistic information regarding the adsorption process. In addition, it can overcome experimental limitations and provide insight into As(V) adsorption and the importance of the ligand functional groups.

In our modeling approach, we model the molecular analogue of the $(TBP)_2Al_{30}$-S crystal structure and compare the DFT energetics of TBP forming attachments through different exposed functional groups on Al_{30}. To probe whether chemically similar arsenate exhibits similar reactivity as phosphate to Al_{30}, the computational studies go on to compare the adsorption of TBP to TBA (t-butylarsenate, $(CH_3)_3CAsO_3$). Furthermore, as both arsenate and phosphate exhibit vast speciation in natural waters, DFT calculations modeling the adsorption of other phosphates, organophosphates, and their As(V) analogues are also performed. In doing so, we are able to identify the sites on Al_{30} that are most reactive toward oxyanion species and demonstrate generality in adsorption trends across a range of P(V) and As(V) speciation. This study continues our previous combined experimental and theoretical investigation of $Cu^{2+}/SO_4{}^{2-}$ co-adsorption to the surface of Al_{30}. Therein, we demonstrated that the semipores in the so-called beltway region of Al_{30} enable enhanced electrostatic interactions between surface functional groups and outer-sphere sulfate ions. The strength of the Al_{30}-$SO_4{}^{2-}$ interaction was shown to correlate with topographical variation in the Al_{30} electrostatic potential.[41,42] Here, we focus on the reactivity of Al_{30} toward polyoxoanion adsorbates, comparisons of phosphate and arsenate analogues, and ligand substitutions of the oxyanions.

■ EXPERIMENTAL SECTION

Synthesis of $(TBP)_2Al_{30}$-S. A partially hydrolyzed aluminum stock solution was prepared by adding 60 mL of a 0.25 M NaOH (6.25 mmol) solution dropwise to 25 mL of 0.25 M $AlCl_3$ (6.25 mmol) at 80 °C. This solution was cooled to room temperature, and a 7 mL aliquot was loaded into a 23 ml Teflon-lined Parr reaction vessel. The vessel was placed in a gravimetric oven at 80 °C to promote additional hydrolysis and formation of the Al_{30} species. After 24 h, the sample was cooled slowly to room temperature, transferred to a glass scintillation vial, and 0.0575 g (0.42 mmol) of TBP was added to the solution. After the resulting solution was stirred for 10 min, a 3 mL aliquot of a 0.1 M 2,6-napthalene disulfonate (2,6-NDS) solution was added as a crystallization agent. A small amount of amorphous flocculants formed upon addition of the 2,6-NDS, and additional stirring was necessary to form a transparent solution. The pH of the final solution was measured at 5.7. After two weeks of slow evaporation, platelike, clear crystals of $(TBP)_2Al_{30}$-S formed on the bottom of the glass vial with yields of 51% based upon Al.

Structural Characterization. Single crystals of $(TBP)_2Al_{30}$-S were separated from the mother liquor, coated in mineral oil (Infinium) and mounted on a Nonius Kappa CCD single crystal X-ray diffractometer equipped with Mo Kα radiation (λ = 0.7107 Å) and a low-temperature cryostat. Data collection, cell refinement, data reduction, and absorption corrections were performed using Collect and APEX II software. The structure was solved using direct methods and refined on the basis of F^2 for all unique data using the Bruker SHELXTL version 6.10 programs. Al, S, and P atoms were located in the direct methods solution, and the O and C atoms were identified in the difference Fourier maps calculated following refinement of the partial-structure models. Selected data collection parameters are given in Table 1, and relevant bond distances for $(TBP)_2Al_{30}$-S are provided in the Supporting Information, Table S1.

$(TBP)_2Al_{30}$-S crystallized in the triclinic space group $P\overline{1}$ with a = 16.249(3) Å, b = 20.213(3) Å, c = 20.859(3) Å, α = 87.323(4)°, β = 73.148(3)°, and γ = 73.918(3)°. H atoms associated with the naphthalene rings of the disulfonate anion were constrained using a riding model. Disorder was present for several of the 2,6-NDS anions due to free rotation about the S−C bond; therefore, O atoms associated with the sulfonate functional group were modeled as split sites with 50% occupancy. The presence of large void space (2725 $Å^3$) within the crystalline lattice also resulted in the presence of disordered solvent (water) molecules. This diffuse electron density was modeled using the SQUEEZE command in the PLATON software,[43] reducing the R_1 value from 21% to 7% and accounting for 1060 electrons within the cavity. The crystallographic information files for $(TBP)_2Al_{30}$-S and additional details and results of the chemical characterization (thermogravimetric analysis, NMR, and IR spectroscopy) of the material are available in the Supporting Information.

Computational Methodology. Computational modeling was performed to compare the experimental $(TBP)_2Al_{30}$-S structure to other adsorption geometries of TBP on Al_{30}. The approach used to solve this problem was to generate a series of isolated aqueous molecular structures with TBP bound through varying Al_{30} surface functional groups. The adsorption geometries were then subjected to geometry optimizations and total energy comparisons. Geometry optimization calculations were performed at the DFT-GGA level,[44] with aqueous effects accounted for by the conductor-like screening model (COSMO) with the dielectric constant chosen to model water to simulate environmental conditions.[45] When using COSMO, the cluster is placed into a cavity within the implicit water as described by the dielectric constant. The charge distribution of the cluster polarizes the dielectric continuum, and the response to the medium is described by screening charges on the caivty's surface. The structural optimizations used a convergence criterion of 0.03 eV/Å. A DNP numerical atom-centered basis set (with a cutoff radius of 3.5 Å) was employed, as implemented in DMol^3.[346,47] Further details of the computational methods (including benchmarking and convergence studies for Al_{30}) are reported in our previous work.[41,42]

The initial isolated molecular structure for Al_{30} was based on the experimental crystal structure, which has been reported previously.[10,12,13] On the basis of bond valence analysis,[48] the molecular formula of Al_{30} is expected to be $(Al_{30}O_8(OH)_{56}(H_2O)_{26})^{18+}$, and the molecule has inversion symmetry. However, as previously reported, DFT vibrational calculations imply that the 18+ form of Al_{30} is unstable. Instead, Al_{30}^{16+} $(Al_{30}O_8(OH)_{58}(H_2O)_{24})^{16+}$ was used as the starting molecular form in the adsorption modeling. To systematically define the adsorption geometries, the functional group naming scheme of Rustad is used, as shown in Figure S7.[49] There are five different water functional groups (ηH_2O) of varying distance from the tetrahedral Al in each end of Al_{30}. A total of three Al_{30}^{16+} species were generated by deprotonating symmetry-equivalent 1, 4, and 5-ηH_2O groups in the 18+ structure, and all were optimized to yield stable structures as confirmed by vibrational analysis. The 16+ form of Al_{30} is also supported by classical molecular dynamics simulations[49] that show the formation of bridged $H_3O_2^-$ groups, also seen in the DFT 16+ molecules resulting from deprotonation of 3/4-ηH_2O groups.

The salient features of the crystal structure were used to guide and constrain the model adsorption geometries considered. As discussed in detail in the Results, the experimental $(TBP)_2Al_{30}$-S structure has each TBP bound covalently to Al_{30} through two ηH_2O functional groups in an inner-sphere bidentate mode. Bond valence analysis of the experimental structure shows that the oxygen atoms of the ηH_2O groups in the adsorbed structure are no longer protonated and instead satisfy their valence through the new bonds formed to the phosphorus atom of TBP. Four models for bidentate adsorption were generated and labeled as $(TBP)_2Al_{30}$ A−D, defined by the identity of the functional groups binding P, as follows: A 3/4-ηH_2O, B 1-ηH_2O, C 2/4-ηH_2O, and D 5-ηH_2O. With the exception of the edge-sharing configuration in D, all of the structural models form corner-sharing, bidentate complexes (as seen in the crystal structure), with the A structure corresponding to the experimental $(TBP)_2Al_{30}$-S geometry. In terms of Al_{30} topography, the A and C structures involve functional groups in the beltway, while the B structure involves functional groups on the caps of the molecule, as can be seen in Figure S7. Arsenate analogues to the four theoretical $(TBP)_2Al_{30}$ A−D structures are also modeled and subjected to full geometry optimization, and they are referred to as $(TBA)_2Al_{30}$ A−D.

The adsorption of four other organophosphate species, namely, methylphosphonate, phenylphosphonate, hydroxyphosphonate, and methoxyphosphonate, was also modeled in the same A−D configurations as those used for TBP adsorption. All adsorption geometries were subjected to DFT geometry optimization, and the total energy information was analyzed. The DFT-optimized geometries of the four acids are shown in Figure 1. Throughout, methylphosphonate is referred to as M, phenylphosphonate as Ph, hydroxyphosphonate as OH, and methoxyphosphonate as OCH_3. The different R groups were chosen to include a range of inductive effects. On the basis of the large positive charge on Al_{30}, it is expected that substituting the ligand with electron-donating R-groups will enhance the reactivity. Comparing the five ligands, the values of E_{rxn} for the five $(RP)_2Al_{30}$ structures are expected to follow the order of $(TBP)_2Al_{30}$ < $(MP)_2Al_{30}$ < $(PhP)_2Al_{30}$ < $(POH)_2Al_{30}$ < $(POCH_3)_2Al_{30}$. The arsenate analogues $(MAs)_2Al_{30}$, $(PhAs)_2Al_{30}$, $(AsOH)_2Al_{30}$, and $(AsOCH_3)_2Al_{30}$ are also modeled, with the same four adsorption sites A−D considered for each.

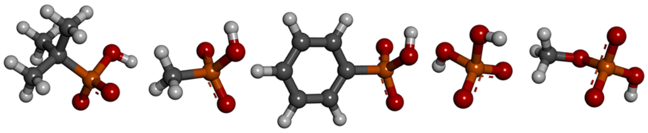

Figure 1. DFT-optimized geometries of the various phosphate species binding to Al_{30} with varying R groups. (left to right) The R groups are *tert*-butyl (TB), methyl (M), benzene (Ph), hydroxyl (OH), and methoxy (OCH_3). The color scheme for the P, O, C, and H atoms are orange, red, black, and gray, respectively.

■ RESULTS AND DISCUSSION

Structural Characterization by Single-Crystal X-ray Diffraction. The core feature of the $(TBP)_2Al_{30}$-S molecule is the Keggin-type aluminum polycation (Figure 2). All Keggin-type species contain the tridecamer (Al_{13}) species with a central AlO_4 tetrahedron surrounded by 12 octahedrally coordinated Al atoms. Al−O bond lengths for the tetrahedrally coordinated Al^{3+} atoms in $(TBP)_2Al_{30}$-S range from 1.776(2) to 1.819(2) Å, whereas the distances for the octahedra are between 1.826(2) and 2.042(3) Å. The exterior Al^{3+} cations are arranged into four $[Al_3(\mu_2\text{-}OH)_6(H_2O)_3]$ units, with each of the trimers connected through bridging hydroxyl groups. Five possible isomers have been identified for Al_{13} Keggin molecules that are based on the orientation and number of shared edges existing between the trimeric units. The ε-Al_{13} isomer is the dominant form present in the partially hydrolyzed aluminum stock solution and can be identified by the formation of edge-sharing hydroxyl groups between the four $[Al_3(\mu_2\text{-}OH)_6(H_2O)_3]$ units. Rotation of one trimer by 60° results in the formation of shared vertices to the neighboring $[Al_3(\mu_2\text{-}OH)_6(H_2O)_3]$ groups and constitutes the δ-Al_{13} isomer. The δ-Al_{13} is prone to additional hydrolysis with soluble monomers, dimers, and neighboring

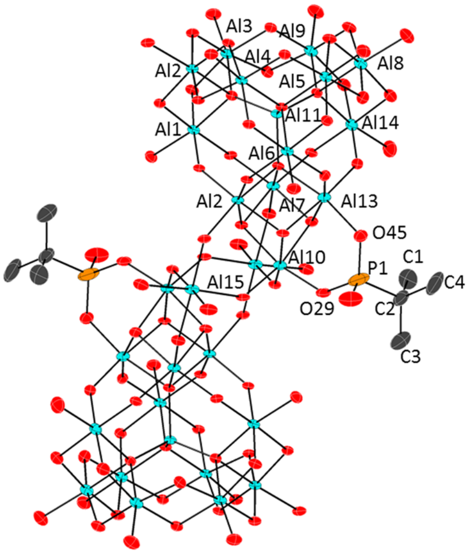

Figure 2. Structural characterization of the experimental $(TBP)_2Al_{30}$-S molecule. Al^{3+} cations are represented by the blue ellipsoids, whereas O, P, and C atoms are indicated by the red, orange, and gray ellipsoids, respectively.

Al_{13} molecules to form larger Al_{30} polynuclear species with the molecular formula $[Al_2(\mu_4\text{-}O_8)(Al_{28}(\mu_2\text{-}OH)_{56}(H_2O)_{26})]^{18+}$. This polycation possesses an hourglass shape, with each of the Al_{13} units forming the exterior caps that narrow through the central beltway region.

Two TBP ligands are bonded to the surface of the Al_{30} molecule through the O atoms of the phosphate functional group, resulting in the formation of a $[(TBP)_2Al_2(\mu_4\text{-}O_8)\text{-}(Al_{28}(\mu_2\text{-}OH)_{56}(H_2O)_{22})]^{14+}$ cation. The phosphate ligands coordinate in the central beltway region and form a bridging bidentate configuration with *tert*-butyl functional group pointed away from the Al_{30} molecule. P—O bond distances within the phosphate group are 1.610(7) Å for the free O atom (O46), while bond lengths for the bridging O atoms are 1.510(3) and 1.519(30) Å for O29 and O45, respectively. Complexation of the TBP molecule on the surface of the Al_{30} polycation also results in contraction of the Al—O bond distance (1.826(3) and 1.853(3) Å for O29 and O45) compared to the ηH_2O groups that are generally observed at ~2.0 Å.

Arrangement of the $(TBP)_2Al_{30}$-S structure into an ordered three-dimensional lattice occurs with the addition of 2,6-NDS as the charge balancing crystallization agent. The sulfonate functional groups participate in H-bonding with the aluminum polycation, and additional $\pi-\pi$ stacking of the naphthalene rings provides a supramolecular interaction that results in the crystallization of the material. Two Cl^- anions and 60 water molecules are also present in the interstitial void spaces, but the solvent molecules are relatively disordered in the crystalline lattice. The resulting $(TBP)_2Al_{30}$-S solid phase has an overall formula of $[(TBP)_2Al_2(\mu_4\text{-}O_8)(Al_{28}(\mu_2\text{-}OH)_{56}(H_2O)_{22})]^{14+}\text{-}(2{,}6\text{-}NDS)_6Cl_2(H_2O)_{60}$.

Structural and mechanistic details between previously reported studies investigating phosphate adsorption on aluminum hydroxide surfaces and the $(TBP)_2Al_{30}$-S molecule are similar. Bridging bidentate coordination of the TBP ligand to the surface of the Al_{30} polycation is identical to the predicted coordination for aluminum oxide and hydroxide surfaces based upon NMR and EXAFS spectroscopies. Li et al., in 2013 observed from ^{31}P NMR data that a peak at 0 ppm corresponds to a deprotonated bridging bidentate configuration and is found to be favored over the monodentate mode on a variety of aluminum oxide and hydroxide surfaces.[33] Rajan also predicted that the adsorption occurs through a terminal water site on the surface of hydrous alumina that would result in lower surface charge.[34] The same result occurs for the adsorption of the TBP molecules to the Al_{30} surface because the binding results from the displacement of a water molecule, lowering the overall charge on the molecule to 14+.

Additional information can be gained from the structural characterization of the $(TBP)_2Al_{30}$-S molecule. First, diffraction data can provide the exact binding site for the phosphate ligand. In this case, the bridging bidentate coordination does not occur at the end members of the Al_{30} molecule but within the beltway region. This site is identical to the position of the bridging bidentate Cu^{2+} adsorption[41] and is also where the greatest solvent and (outer-sphere) anion densities were reported in classical molecular dynamics simulations of Al_{30} by Rustad.[49] Second, structural models have previously reported atomic distances for bidentate phosphate surface complexes, predicting that Al—P distances should be 3.1 Å, which is slightly longer than the values observed by X-ray diffraction of 3.01 and 3.06 Å.[50] The discrepancy may arise from the presence of the *tert*-butyl functional group, but differential pair distribution function analysis of high-energy X-ray scattering data on arsenate adsorbed to γ-alumina found As—O and As—Al atomic pair correlations of 1.66 and 3.09 Å.[51] Additional DFT calculations theorize that these atomic distances corresponded to a bridging bidentate coordination. As the As(V) atom (r = 0.34 Å) is larger than the P(V) (r = 0.29 Å) atom, the value observed by X-ray diffraction for the Al—P distance is likely more accurate.[51]

Computational Analysis. The $(TBP)_2Al_{30}$-S molecule can be described as a contact ion pair between the cationic Al_{30} and anionic TBP. Following the discussion of Casey and Rustad[52] on the formation of analogous ion pairs between fluoride and the Al_{13} polycation, we consider the Eigen—Wilkens (EW) mechanism[53−55] that proceeds by the initial formation of an outer-sphere ion pair followed by ligand exchange to form the final product as shown in Scheme 1 and depicted molecularly in Figure 3. DFT reaction energies E_{rxn} are then calculated from the net reaction in Scheme 1 and using the total energy information for each reactant and product species, weighted by the appropriate stoichiometric coefficients. The minimum value of E_{rxn} is used to predict which $(TBP)_2Al_{30}$ structure is energetically preferred. For the modeled addition of different organophosphate, values of E_{rxn} were calculated based on the net reaction of Scheme 1 modified to include the appropriate

Scheme 1. Eigen—Wilkens Mechanism That Proceeds by the Initial Formation of an Outer-Sphere Ion Pair Followed by Ligand Exchange to Form the Final Product

Step 1: Ion-Pair Formation

$$Al_{30}O_8(OH)_{56}(H_2O)_{22} - (OH)_2(H_2O)_2^{16+} + 2\,RXO_2OH^{1-} \rightarrow [Al_{30}O_8(OH)_{56}(H_2O)_{22} - (OH)_2(H_2O)_2^{16+}, 2\,RXO_2OH^{1-}]^{14+}$$

Outer-sphere ion pair

Step 2: Ligand-Exchange

$$[Al_{30}O_8(OH)_{56}(H_2O)_{22} - (OH)_2(H_2O)_2^{16+}, 2\,RXO_2OH^{1-}]^{14+} \rightarrow Al_{30}O_8(OH)_{56}(H_2O)_{22} - (RXO_2O)_2^{14+} + 4\,H_2O$$

Net Reaction

$$Al_{30}O_8(OH)_{56}(H_2O)_{22} - (OH)_2(H_2O)_2^{16+} + 2\,RXO_2OH^{1-} \rightarrow Al_{30}O_8(OH)_{56}(H_2O)_{22} - (RXO_2O)_2^{14+} + 4\,H_2O\}$$

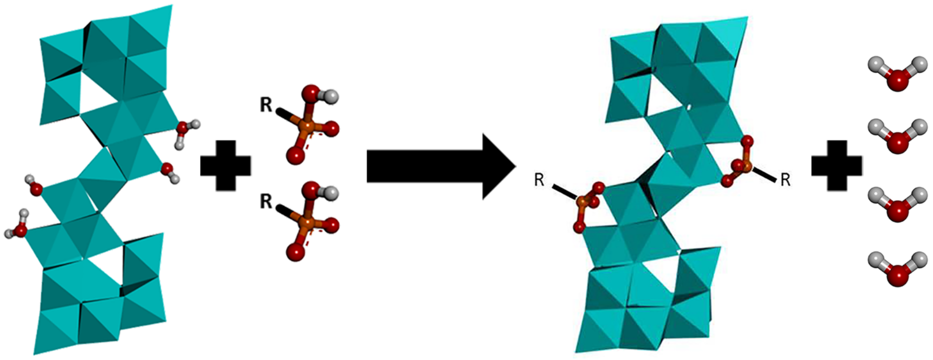

Figure 3. A graphical depiction of the adsorption reaction of phosphate and arsenate species to Al_{30} to form $(RX)_2Al_{30}$ following the net reaction shown in Scheme 1. R represents the ligand bound to P/As. The Al_{30} polycation is shown in a polyhedral representation with the reactive functional groups shown in a ball-and-stick representation. AlO_6/AlO_4 octahedra/tetrahedra are shown in blue, while P, O, and H atoms are represented by orange, red, and gray spheres, respectively. The R groups examined include *tert*-butyl (TB), methyl (M), benzene (Ph), hydroxyl (OH), and methoxy (OCH_3).

singly deprotonated phosphonic acid (methylphosphonic acid ($CH_3CPO_2OH^{1-}$), phenylphosphonic acid ((C_6H_5)-CPO_2OH^{1-}), hydroxyphosphonic acid ($OHCPO_2OH^{1-}$), and methoxyphosphonic acid ($OCH_3CPO_2OH^{1-}$)). Values of E_{rxn} for the addition of different oraganoarsenates were similarly calculated.

Calculated values of E_{rxn} are used to probe the relative reactivity of the modeled adsorption sites on Al_{30}. The results (Table 2, calculated based on the net reaction shown in Scheme 1 then divided by two to represent the energy per adsorbate) show that the theoretically preferred adsorption geometry for all species is C. However, the difference between the values of E_{rxn} for the A and C structures (both with adsorption in the beltway region) is less than 0.20 eV (4.6 kcal/mol) in all cases, and thus the two sites are essentially degenerate within the accuracy of the DFT methods employed. On the other hand, the differences in values of E_{rxn} for the A structures (beltway adsorption) compared to the B structures (cap adsorption) are relatively large for all adsorbing species, with the A structure preferred by 0.27−0.36 eV and 0.32−0.51 eV for the various phosphate and arsenate adsorbates, respectively. This highlights the distinction of adsorption sites in terms of Al_{30} topography and the exceptional reactivity of the Al_{30} beltway. The D site, as noted, is an edge-sharing configuration, and has E_{rxn} values that are unfavorable by 0.35−0.62 eV and 0.44−0.47 eV compared to the A structure for the various phosphate and arsenate adsorbates, respectively. We therefore focus on the distinction between the beltway adsorption geometries (A and C) compared to the B structure, which has adsorption occurring on the caps of Al_{30}.

Table 2. Calculated Values of E_{rxn} of Various Phosphate and Arsenate Species As Defined in the Text

E_{rxn} (eV)	A	B	C	D
$(TBP)_2Al_{30}$	−1.05	−0.73	−1.25	−0.43
$(MP)_2Al_{30}$	−1.03	−0.67	−1.20	−0.41
$(PhP)_2Al_{30}$	−0.92	−0.58	−1.04	−0.30
$(POH)_2Al_{30}$	−0.87	−0.57	−1.05	−0.52
$(POCH_3)_2Al_{30}$	−0.80	−0.53	−1.00	−0.24
$(TBAs)_2Al_{30}$	−1.39	−0.88	−1.50	−0.92
$(MAs)_2Al_{30}$	−1.38	−0.87	−1.49	−0.91
$(PhAs)_2Al_{30}$	−1.23	−0.73	−1.31	−0.76
$(AsOH)_2Al_{30}$	−0.91	−0.58	−1.03	−0.47
$(AsOCH_3)_2Al_{30}$	−0.90	−0.58	−1.06	−0.46

While it was anticipated that the inductive effects of varying R-groups on the ligands would tune reactivity, only a subtle effect is reflected in the values of E_{rxn}. Comparing the TB and

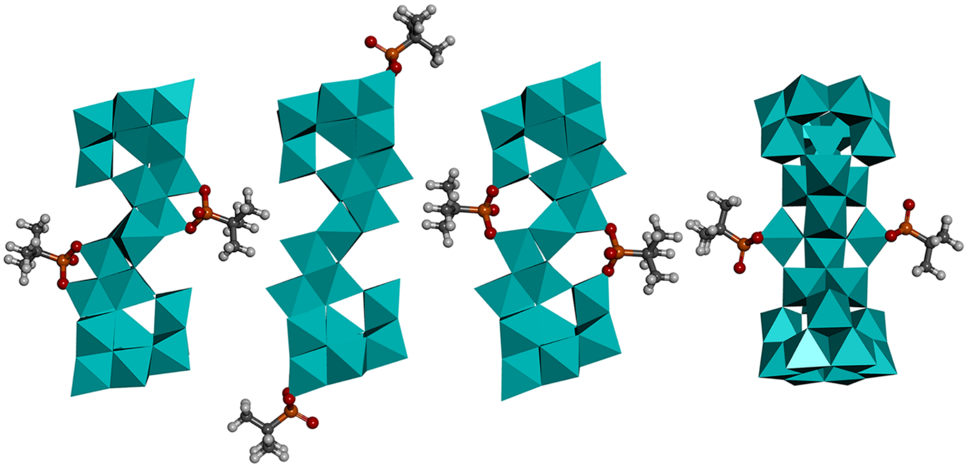

Figure 4. DFT-optimized geometries of the modeled $(TBP)_2Al_{30}$ structures. (left to right) A, B, C, and D structures (defined in the text) are shown. AlO_6/AlO_4 octahedra/tetrahedra are shown in blue, while P, O, C, and H atoms are represented by orange, red, black, and gray spheres, respectively.

OCH_3 ligand for the A site structures, the values of E_{rxn} for P vary by 0.25 eV, while for As the variation is 0.49 eV. The similarities in values of E_{rxn} between the R-substituted anions can be viewed as evidence that the preference to adsorb in the beltway region persists over a range of P or As speciation.

Optimized geometries for all four configurations of $(TBP)_2Al_{30}$ are shown in Figure 4, and key bond distances are compared to the experimental values in Table 3.

Table 3. Key Bond Distances As Defined in the Text for the Experimental $(TBP)_2Al_{30}$-S Structure and the Computational $(TBP)_2Al_{30}$ and $(TBAs)_2Al_{30}$ Structures

P/As distances (Å)	expt	A	B	C	D
d(P−O)	1.610	1.558	1.527	1.540	1.525
$d(P-O_{Al_{30}})$	1.515	1.588	1.595	1.596	1.600
d(As−O)		1.751	1.701	1.741	1.724
$d(As-O_{Al_{30}})$		1.760	1.773	1.753	1.775

Specifically, we report on the distance between the P and bridging oxo groups of Al_{30} as well as the distance between the P and the unshared O atom of the phosphate group d(P−O). The experimental structure and the theoretical structures are in reasonable agreement. For example the distance between phosphorus and the bridging oxo groups of Al_{30}, $d(P-O_{Al_{30}})$, differs by 0.073 Å for the A site and 0.081 Å for the C site when compared to the experimental crystal structure. Geometry analysis also provides a possible explanation for the unfavorable value of E_{rxn} at the D site, in which the oxyanions adsorb in an edge-sharing configuration. The angle between the adsorption sites and the P shows that the angle in the $(TBP)_2Al_{30}$-D structure is 14.7% smaller compared to the experimental structure, shown in Table 4, which implies that the edge-sharing configuration is sterically unfavorable. Key bond distances and bond angles for the arsenic analogue $(TBAs)_2Al_{30}$ structures A−D are also reported in Tables 3 and 4, while the $(TBP)_2Al_{30}$-A structure is shown in Figure 5. The distance between the arsenic and bridging oxo groups of Al_{30} as well as the distance between the arsenic and the unshared O atom of the arsenate group of the $(TBP)_2Al_{30}$-A configuration are longer than its crystal structure P analogue by 0.172 Å. In addition, the distance between arsenic and the bridging oxo groups of Al_{30} differs by 0.245 Å for the A site when compared to the $(TBP)_2Al_{30}$-S crystal structure. Elongation of the bond lengths is expected because the radius of As (0.34 Å) is larger than that of P (0.29 Å). Once again the ∠O−As−O is much smaller for the D structure (91.02°) compared to the corner-sharing structures.

Table 4. Key Bond Angles As Defined in the Text for the Experimental $(TBP)_2Al_{30}$-S Structure and the Computational $(TBP)_2Al_{30}$ and $(TBAs)_2Al_{30}$ Structures

angles (deg)	expt	A	B	C	D
$\angle(O_{Al_{30}}-P-O_{Al_{30}})$	113.75	107.15	108.12	109.87	97.00
$\angle(O_{Al_{30}}-As-O_{Al_{30}})$		104.82	106.10	109.56	91.02

The trends in E_{rxn} and the structural details presented suggest similar adsorption behavior between phosphates and arsenates. To further compare P and As adsorption, we visualize the P/As adsorption-induced charged density. The induced charge density is denoted as $\Delta\rho_{P/As}$ and taken as $\rho_{(TBX)_2Al_{30}} - \rho_{Al_{30}} - \rho_{TBX}$, $\Delta\rho_{P/As}$. Plots of $\Delta\rho_{P/As}$ are shown for $(TBP)_2Al_{30}$-A and $(TBAs)_2Al_{30}$-A in Figure 6. The qualitative agreement in $\Delta\rho_{P/As}$ for both polyoxoanions further supports that experimental results for phosphates may be extrapolated to arsenate. We also note that the *tert*-butyl ligand is not covered by the $\Delta\rho_{P/As}$ isosurface. This supports that the identity of the functional group does not play a major role in P/As reactivity with Al_{30}. Details of the optimized geometries for the A structures of the various organophosphate adsorption structures and arsenate analogue species are reported in Table 5. The A structures for phosphate adsorption are shown in Figure 7 and appear similar to the arsenate analogues. The distance between the P/As and the R group (connecting C in the R group for TB, M, and Ph and connecting O in the R group for OH and OCH_3) is denoted as d(P/As−R), while the distance between the P/As and the bridging oxo groups of Al_{30} is denoted as $d(P/As-O_{Al_{30}})$. Variation of the P/As−R bond is observed over the range of R groups. Larger R groups have longer P/As−R bond distances, while the smaller R groups have slightly shorter P/As−R distances. The greatest difference in d(P/As−R) for either P or As is between TB and OCH_3 with the former being at least 0.2 Å longer.

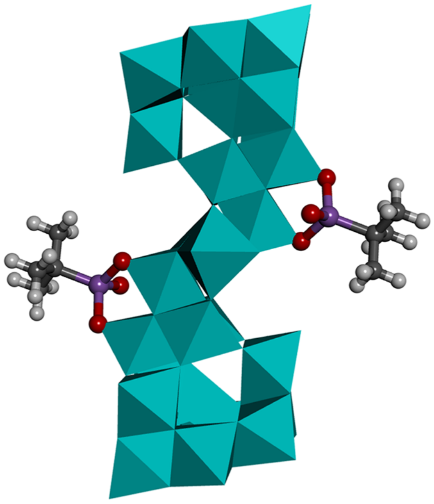

Figure 5. DFT-optimized geometry of the $(TBAs)_2Al_{30}$ A configuration. The representation of species is the same as in Figure 4 with As shown in purple spheres.

To further rationalize the subtle variations in E_{rxn} as a function of R group substitution of the oxyanions, we analyze the Mulliken charge population values.[56] In particular, we monitor $\Delta(RX)_2Al_{30}$-R, the difference between the Mulliken charge on P/As in the $(RX)_2Al_{30}$ structures and the value in the corresponding isolated polyoxoanion form. Table 6 shows that the $\Delta(RX)_2Al_{30}$ values differ by only 0.03 charge units for all of the phosphates and 0.04 charge units for all of the arsenates. This further supports that adsorption behavior is not strongly dependent on speciation and that phosphate and arsenate interact with Al_{30} similarly.

■ CONCLUSIONS

The experimental structural characterization of $(TBP)_2Al_{30}$-S shows that an inner-sphere ion pair between TBP and Al_{30} forms via adsorption in the beltway region of the polycation. Complementary computational studies of R-substituted phosphate and arsenate species adsorbing to Al_{30} provide evidence for a shape−reactivity relationship in the Al_{30}

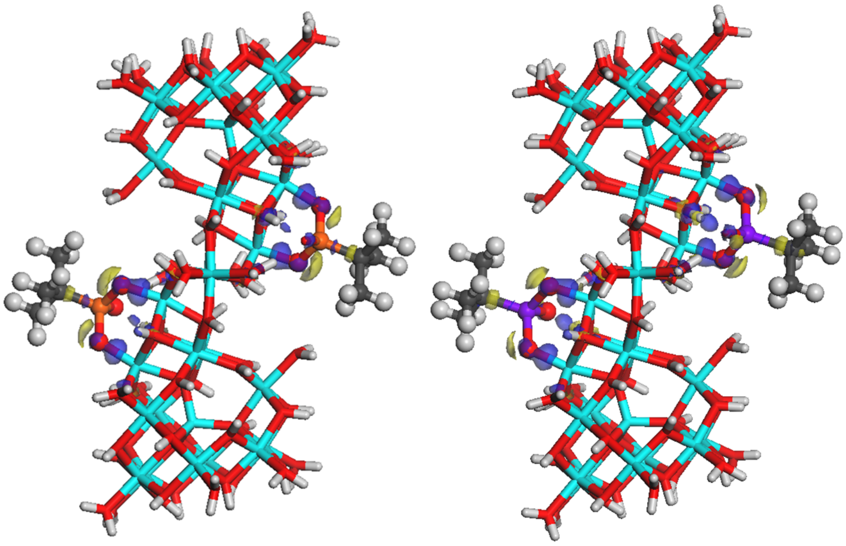

Figure 6. Induced density $\Delta\rho_{P/As}$ for the $(TBP)_2Al_{30}$–A and $(TBAs)_2Al_{30}$–A structures. Charge loss is shown in blue, and charge gain is shown in yellow. The color scheme for the P, As, Al, O, C, and H atoms is orange, purple, blue, red, black, and gray, respectively.

Table 5. Key Bond Distances As Defined in the Text for the Computational $(RP)_2Al_{30}$ and $(RAs)_2Al_{30}$ Structures for Each R Group for the A Site

P/As distances (Å)	TB	M	Ph	OH	OCH_3
$d(P–R)$	1.828	1.787	1.793	1.603	1.600
$d(P–O_{Al_{30}})$	1.588	1.587	1.587	1.577	1.576
$d(As–R)$	1.989	1.921	1.917	1.767	1.769
$d(As–O_{Al_{30}})$	1.760	1.758	1.759	1.745	1.745

Table 6. Values of $\Delta(RX)_2Al_{30}$-R[a]

$\Delta(RX)_2Al_{30}$-R (charge units)	TB	M	Ph	OH	OCH_3
P	0.18	0.15	0.17	0.15	0.14
As	0.13	0.14	0.16	0.12	0.10

[a] The difference between the Mulliken charge on P/As in the $(RX)_2Al_{30}$ structures and the value in the corresponding isolated polyoxoanion form. Values are reported in units of fundamental charge.

polycation. Specifically, the distinction of adsorption sites in terms of the molecular topography (i.e., "beltway" vs "cap" sites on Al_{30}) and electrostatic properties of the polycation are shown to be reliable predictors of adsorption trends on the polycation surface. Our previous studies have revealed strong outer-sphere ion pair formation for ions in the beltway.[42] Extending this knowledge to the $(TBP)_2Al_{30}$-S structure, we intuit that Step 1 of the EW mechanism (Scheme 1) drives the beltway site preference, and subsequent ligand exchange then results in the final inner-sphere ion pair. It is noteworthy that oxygen functional group type and coordination alone cannot explain the greater reactivity of adsorption sites in the Al_{30} beltway region, even though such arguments have been successfully applied to a variety of mineral surface reactivities. This result motivates ongoing research to converge the well-described structure–reactivity relationships of mineral surfaces with the apparent shape–reactivity relationship in Keggin-based molecular geochemical models.

■ ASSOCIATED CONTENT

Ⓢ Supporting Information

The Supporting Information is available free of charge on the ACS Publications website at DOI: 10.1021/acs.inorgchem.5b01039.

Table of bond lengths and angles, Al-27 and P-31 NMR, TGA, IR, additional details on computational methods (PDF)

CIF file with crystallographic structure illustrated (CIF)

■ AUTHOR INFORMATION

Corresponding Authors

*E-mail: tori-forbes@uiowa.edu. (T.Z.F.)

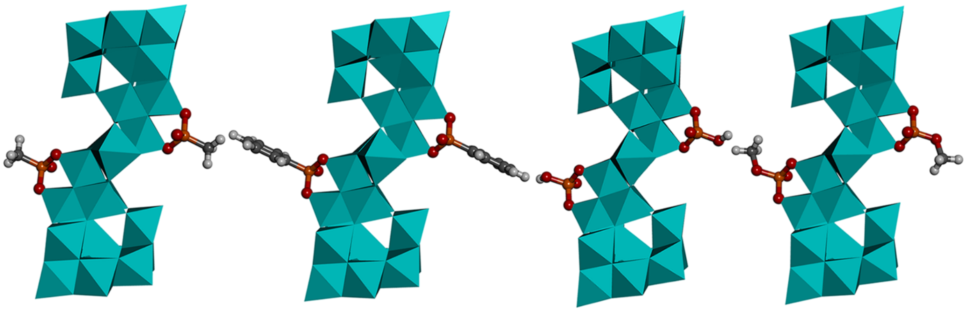

Figure 7. A configurations of the $(RP)_2Al_{30}$ structures computationally modeled. (left to right) $(MP)_2Al_{30}$, $(PhP)_2Al_{30}$, $(POH)_2Al_{30}$, and $(POCH_3)_2Al_{30}$. The representation of species is the same as in Figure 4.

*E-mail: sara-mason@uiowa.edu. (S.E.M.)

Notes

The authors declare no competing financial interest.

ACKNOWLEDGMENTS

S.E.M. acknowledges support from NSF Grant No. CHE-1254127, and both S.E.M and T.Z.F thank the Univ. of Iowa College of Liberal Arts and Sciences for initial funding. We would like to thank the UI NMR Facility and F. Chen for his help collecting the Al-27 and P-31 NMR spectra.

REFERENCES

(1) Casey, W. H.; Phillips, B. L.; Furrer, G. *Rev. Mineral. Geochem.* **2001**, *44*, 167.

(2) Baes, C. F.; Mesmer, R. E. *The hydrolysis of cations;* John Wiley and Sons: New York, NY, 1976.

(3) Casey, W. H. *Chem. Rev.* **2006**, *106*, 1.

(4) Jolivet, J.-P.; Chaneac, C.; Chiche, D.; Cassaignon, S.; Durupthy, O.; Hernandez, J. *C. R. Geosci.* **2011**, *343*, 113.

(5) Heath, S. L.; Jordan, P. A.; Johnson, I. D.; Moore, G. R.; Powell, A. K.; Helliwell, M. *J. Inorg. Biochem.* **1995**, *59*, 785.

(6) Akitt, J. W.; Elders, J. M. *J. Chem. Soc., Faraday Trans. 1* **1985**, *81*, 1923.

(7) Akitt, J. W.; Farthing, A. *J. Chem. Soc., Dalton Trans.* **1981**, 1624.

(8) Wang, W.; Wentz, K. M.; Hayes, S. E.; Johnson, D. W.; Keszler, D. A. *Inorg. Chem.* **2011**, *50*, 4683.

(9) Johansson, G. *Acta Chem. Scand.* **1960**, *14*, 771.

(10) Abeysinghe, S.; Unruh, D. K.; Forbes, T. Z. *Cryst. Growth Des.* **2012**, *12*, 2044.

(11) Sun, Z.; Wang, H.; Tong, H.; Sun, S. *Inorg. Chem.* **2011**, *50*, 559.

(12) Allouche, L.; Gerardin, C.; Loiseau, T.; Ferey, G.; Taulelle, F. *Angew. Chem., Int. Ed.* **2000**, *39*, 511.

(13) Rowsell, J.; Nazar, L. F. *J. Am. Chem. Soc.* **2000**, *122*, 3777.

(14) Stewart, T. A.; Trudell, D. E.; Alam, T. M.; Ohlin, C. A.; Lawler, C.; Casey, W. H.; Jett, S.; Nyman, M. *Environ. Sci. Technol.* **2009**, *43*, 5416.

(15) Yan, M. Q.; Wang, D. S.; Yu, J. F.; Ni, J. R.; Edwards, M.; Qu, H. H. *Chemosphere* **2008**, *71*, 1665.

(16) Carrio, J. A. G.; Faldini, S. B.; de Miranda, L. F.; Kiyohara, P. K.; Silva, L. G. A.; Munhoz, A. H. *Z. Kristallogr.* **2007**, *2007*, 537.

(17) Chen, Z.; Fan, B.; Peng, X.; Zhang, Z.; Fan, J.; Luan, Z. *Chemosphere* **2006**, *64*, 912.

(18) Kang, M.; Kamei, T.; Magara, Y. *Water Res.* **2003**, *37*, 4171.

(19) Fu, G.; Nazar, L. F.; Bain, A. D. *Chem. Mater.* **1991**, 3, 602.

(20) Teagarden, D. L.; Hem, S. L.; White, J. L. *J. Soc. Cosmet. Chem.* **1982**, *33*, 281.

(21) Mertens, J. *Rev. Environ. Sci. Bio/Technol.* **2011**, *10*, 111.

(22) Mertens, J.; Rose, J.; Kagi, R.; Chaurand, P.; Plotze, M.; Wehrli, B.; Furrer, G. *Environ. Sci. Technol.* **2012**, *46*, 7310.

(23) Tilman, D.; Fargione, J.; Wolff, B.; D'Antonio, C.; Dobson, A.; Howarth, R.; Schindler, D.; Schlesinger, W. H.; Simberloff, D.; Swackhamer, D. *Science* **2001**, *292*, 281.

(24) Liu, S. Q.; Jing, C. Y.; Meng, X. Q. *Sci. Total Environ.* **2008**, *392*, 137.

(25) Goldberg, S.; Johnston, C. T. *J. Colloid Interface Sci.* **2001**, *234*, 204.

(26) Ilgen, A. G.; Foster, A. L.; Trainor, T. P. *Geochim. Cosmochim. Acta* **2012**, *94*, 128.

(27) Wilson, S. C.; Lockwood, P. V.; Ashley, P. M.; Tighe, M. *Environ. Pollut.* **2010**, *158*, 1169.

(28) Read, E. K.; Ivancic, M.; Hanson, P.; Cade-Menun, B. J.; McMahon, K. D. *Water Res.* **2014**, *62*, 229.

(29) McLaren, R. G.; Megharaj, J.; Naidu, R. In *Managing Arsenic in the Environment: From Soil to Human Health;* Naidu, R., Smith, E., Owens, G., Bhattacharya, P., Nadebaum, P., Eds.; Csiro Publishing: Collingwood, Australia, 2006; p 157.

(30) ATSDR (Agency for Toxic Substances and Disease Registry) *Toxicological Profile for Arsenic* (Update; Draft for Public Comment); ATSDR: Atlanta, GA, 2007b.

(31) Genc, H.; Tjell, J. C.; McConchie, D.; Schuiling, O. *J. Colloid Interface Sci.* **2003**, *264*, 327.

(32) Mohan, D.; Pittman, C. U. *J. Hazard. Mater.* **2007**, *142*, 1.

(33) Li, W.; Feng, X. H.; Yan, Y. P.; Sparks, D. L.; Phillips, B. L. *Environ. Sci. Technol.* **2013**, *47*, 8308.

(34) Rajan, S. S. S. *Nature* **1976**, *262*, 45.

(35) Kim, Y.; Kirkpatrick, R. J. *Eur. J. Soil Sci.* **2004**, *55*, 243.

(36) Ruttenberg, K. C.; Sulak, D. J. *Geochim. Cosmochim. Acta* **2011**, *75*, 4095.

(37) Yan, Y. P.; Liu, F.; Li, W.; Liu, F.; Feng, X. H.; Sparks, D. L. *Eur. J. Soil. Sci.* **2014**, *65*, 308.

(38) Jing, C. Y.; Liu, S. Q.; Patel, M.; Meng, X. G. *Environ. Sci. Technol.* **2005**, *39*, 5481.

(39) Li, Z. J.; Deng, S. B.; Yu, G.; Huang, J.; Lim, V. C. *Chem. Eng. J.* **2010**, *161*, 106.

(40) Mertens, J.; Casentini, B.; Masion, A.; Pothig, R.; Wehrli, B.; Furrer, G. *Water Res.* **2012**, *46*, 53.

(41) Abeysinghe, S.; Corum, K. W.; Neff, D. L.; Mason, S. E.; Forbes, T. Z. *Langmuir* **2013**, *29*, 14124.

(42) Corum, K. W.; Mason, S. E. *Mol. Simul.* **2015**, *41*, 146.

(43) Spek, A. L. *PLATON, A Multipurpose Crystallographic Tool;* Utrecht University: Utrecht, The Netherlands, 2005.

(44) Perdew, J. P.; Burke, K.; Ernzerhof, M. *Phys. Rev. Lett.* **1996**, *77*, 3865.

(45) Klamt, A.; Schuurmann, G. *J. Chem. Soc., Perkin Trans. 2* **1993**, 799.

(46) Delley, B. *J. Chem. Phys.* **1990**, *92*, 508.

(47) Delley, B. *J. Chem. Phys.* **2000**, *113*, 7756.

(48) Brown, I. D.; Shannon, R. D. *Acta Crystallogr., Sect. A: Cryst. Phys., Diffr., Theor. Gen. Crystallogr.* **1973**, *A29*, 266.

(49) Rustad, J. R. *Geochim. Cosmochim. Acta* **2005**, *69*, 4397.

(50) Li, W.; Feng, X.; Yan, Y.; Sparks, D. L.; Phillips, B. L. *Environ. Sci. Technol.* **2013**, *47*, 8308.

(51) Li, W.; Harrington, R.; Tang, Y.; Kubicki, J. D.; Aryanpour, M.; Reeder, R. J.; Parise, J. B.; Phillips, B. L. *Environ. Sci. Technol.* **2011**, *45*, 9687.

(52) Casey, W. H.; Rustad, J. R. *Annu. Rev. Earth Planet. Sci.* **2007**, *35*, 21.

(53) Wilkins, R. G. *The study of kinetics and mechanism of reactions of transition metal complexes;* Allyn and Bacon, Inc, Boston, MA, 1974.

(54) Burgess, J. *Metal Ions in Solution;* Ellis Horwood Ltd: Chichester, U.K., 1978.

(55) Margerum, D. W.; Cayley, G. R.; Weatherburn, D. C.; Pagenkopf, G. K. *Coordination Chemistry;* Martell, A. E., Ed.; ACS Monograph Series 174; American Chemical Society: Washington, D.C., 1978; Vol. 2, p 1.

(56) Mulliken, R. S.; Rieke, C. A.; Orloff, D.; Orloff, H. *J. Chem. Phys.* **1949**, *17*, 1248.